

# Extending Laboratory BRDF Measurements towards Radiometric Modeling of Resident Space Object Spectral Signature Mixing

GREGORY BADURA,<sup>1</sup> ELENA PLIS,<sup>1</sup> CHRISTOPHER R. VALENTA,<sup>1</sup>

<sup>1</sup>*Georgia Tech Research Institute, Atlanta GA*

## ABSTRACT

The identification of unresolved resident space object (RSO) material composition via imaging spectrometry techniques requires knowledge of the constituent material's directional reflectance characteristics and knowledge of how these directional signatures will mix within the chosen sensor bandpass. In addition, knowledge is required regarding how the directional reflectance changes due to in-orbit aging in order to make use of these datasets in empirically collected measurement campaigns. In this study, we present the design of a principal plane goniometer that is responsive to spectral radiance between 400 and 2400 nm and a method for acquiring spectral bidirectional reflectance distribution function (sBRDF) measurements using the system. Initial sBRDF results for 20 different spacecraft materials of interest are presented for a variety of illumination and observational geometries as a first step towards building a robust database of sBRDF measurements as a function of in-orbit aging time. A two-step BRDF model inversion of the theoretical Ward sBRDF model was performed using the sBRDF data-sets in order to derive model parameters that can be ingested by radiometric modeling tools such as the Digital Imaging and Remote Sensing Image Generation (DIRSIG) model. These radiometric modeling tools were then utilized to model the at-aperture spectral radiance when imaging unresolved mixtures of the materials as a function of varying observer and solar illumination angles for sensor bandpasses of interest to the Space Domain Awareness (SDA) community. Other applications of the methods developed towards efforts such as training machine learning frameworks on radiometrically-accurate resolved imagery and using unsupervised machine learning techniques to perform spectral un-mixing are discussed and presented.

*Keywords:* Spectral Bidirectional Reflectance Distribution Function (sBRDF), Spectroscopy, Modeling & Simulation, Machine Learning, Material Characterization

## 1. INTRODUCTION

Reflectance spectroscopy is a powerful technique for inferring the material composition of both man-made and natural objects (Clark et al. 2003, 2010; Kokaly et al. 2009; Beveridge et al. 2001). This well-established technique allows planetary geologists to investigate the mineralogical compo-

Corresponding author: Gregory Badura  
[gregory.badura@gtri.gatech.edu](mailto:gregory.badura@gtri.gatech.edu)

sition of asteroids and stellar bodies based on comparison of reflectance signatures across multiple photometric bands (Gaffey et al. 1993; Sparks & Ford 2002; Denevi 2011; Clegg et al. 2013). In recent years, results in utilizing visible through shortwave-infrared wavelength spectroscopy to determine the surface material composition of artificial Earth-orbiting objects have begun to show significant promise (Bédard et al. 2015; Gazak et al. 2020; Cowardin et al. 2020).

While there has been recent success in utilizing reflectance spectroscopy to infer resident space object (RSO) properties, the use of this technique in the Space Domain Awareness (SDA) community is still very much a new concept, as was summarized in a study performed by Bédard et al. (2015). In order to advance the use of photometry and spectroscopy for spacecraft material identification, advanced radiometric modeling techniques that are capable of modeling the directional reflectance signatures of RSOs are necessary. In this study, we present approaches for generating machine learning datasets of resolved and unresolved photometric imagery of satellites using physically realistic bidirectional reflectance distribution function (BRDF) modeling within photometric channels of interest. These techniques can be used in order to train machine learning frameworks on tasks such as differentiating between RSOs based on an unresolved BRDF signatures, or training machine learning frameworks to recognize the pose of RSOs in resolved imagery. We also make significant progress towards generating a wide catalog of BRDF measurements of satellite materials that can be used in future studies.

The paper begins with an overview of a principal plane goniometer system that was developed for measuring the directional reflectance of pristine samples in Section 2. Section 3 then presents algorithms for inverting the empirical directional reflectance measurements in order to obtain parameters of theoretical BRDF models that can be ingested by radiometric modeling environments. Section 4 then presents a summary of our implementation of methods for using these derived parameters in the DIRSIG radiometric modeling tool in order to produce radiometrically accurate signatures of RSOs of interest. Finally, a brief discussion of our results for all of these tasks are presented in Section 5 for a representative sampling of the 20 different materials that were measured in this study.

## 2. BRDF MEASUREMENT AND DATA PROCESSING

In an ideal scenario, our goniometer system would measure the bidirectional reflectance distribution function (BRDF) of the samples of interest. A diagram of the concept of BRDF can be seen in Figure 1 (a), in which incident and exitant radiance both have infinitesimal extents to their subtended solid angles, mimicking a “ray-like” phenomena. In many experimental setups, factors such as maximizing signal-to-noise ratios of the data limit the ability to design a system in this manner.

Our system is designed using a light source and receiver fore-optic that both have a finite angular extent. For this reason, we state that our system measures biconical reflectance factor (BCRF) measurements of the sample of interest (Schaepman-Strub et al. 2006). A diagram of the concept of BCRF can be seen in Figure 1 (b), in which the incident source beam has a subtended solid angle of  $\Omega_b$ , and the receiver fore-optic has a subtended solid angle of  $\Omega_{fo}$ .

Our system is designed around an Analytical Spectral Devices (ASD), Inc. FieldSpec 4 Hi-Res spectroradiometer. The spectrometer contains three detectors spanning the spectral range of 350 to 2500 nm: a silicon array for the visible and near-infrared (VNIR) spectral range of 350 to 1000 nm, and two cooled InGaAs photodiode detectors for the short-wave infrared (SWIR) ranges of 1001 to 1800 nm and 1801 to 2500 nm. These systems were calibrated by the manufacturer to provide resolutions of 3 nm in the VNIR and 8 nm in the SWIR. In addition, this spectrometer is able

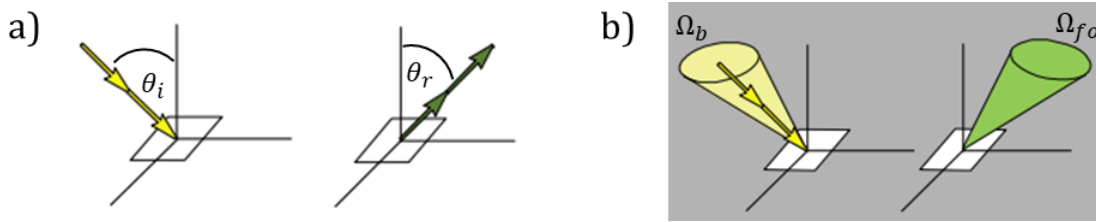


**Figure 1.** A comparison of (a) bidirectional reflectance distribution function (BRDF) and (b) bidirectional conical reflectance factor (BCRF). The yellow indicates the incident radiance while the green indicates received radiance.

to achieve wavelength accuracy of 0.5 nm and wavelength reproducibility to within 0.1 nm. The manufacturer radiometric calibration for the spectrometers results in an absolute radiance accuracy typically 2.5% between 600 and 2400 nm.

The developed system also relies upon a custom-designed light source that shines collimated light onto the target. The light source optical assembly is outlined fully in Section 2.1 and characterized in Appendix A. The critical component of the assembly is the tungsten-halogen MR-16 bulb that provides blackbody irradiance onto the target over the range of 350-2500 nm, matching the measurement range of the spectrometer.

### 2.1. Light Source Design and Characterization

A diagram of the optical assembly of the light source developed for our goniometer system is shown in Figure 2. The light source is a 50-watt MR16 tungsten halogen lamp with a parabolic reflector, which has been used in BRDF studies to simulate a solar blackbody spectrum across the sampled spectral range of 350 nm to 2500 nm (Harms et al. 2017). The beam structure is made Gaussian using a ground glass diffuser, gathered by an aspheric condenser lens to form an approximate point source, and then collimated by a camera lens with a focal length of 50 mm focused at infinity. The light source was attached to a voltage control system in order to avoid intensity fluctuations over the duration of the measurements.

This optical assembly was inspired by previous work in the computer graphics domain performed by Li et al. (2006). The difference in our design is that there is no variable aperture placed between the aspheric lens and the camera lens. While this would improve the point source approximation, the loss of incident radiance onto the target was deemed too great for this study.

An important metric for post-processing the measured sample radiance into the form of BCRF is the solid angle of the light source. A method for characterizing the solid angle of our optical assembly is outlined in the Appendix. Using this method, the solid angle extent of the light source was found to be approximately 0.03 steradians.

### 2.2. BCRF Data Collection

In the process of measuring the BCRF of a material sample as a function of incident source direction,  $(\theta_i, \phi_i)$ , and exitant viewing direction,  $(\theta_r, \phi_r)$ , there are two components that must be evaluated:

1. The incident irradiance onto the targeted object as a function of incident light direction.
2. The received sample radiance by that is reflected by the sample onto the the sensor fore-optic.

In this section, we outline the derivation of BCRF and the scheme for measuring these two components of the sample BCRF. Note that for our simple goniometer system, all measurements are made in

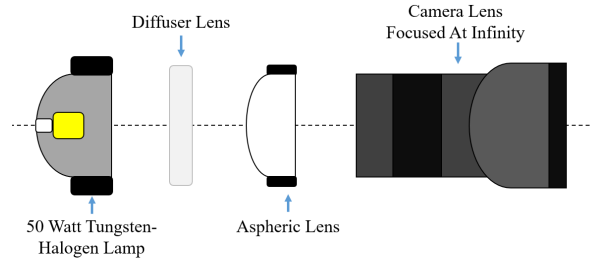


**Figure 2.** Diagram of the light source optical assembly used in this study.

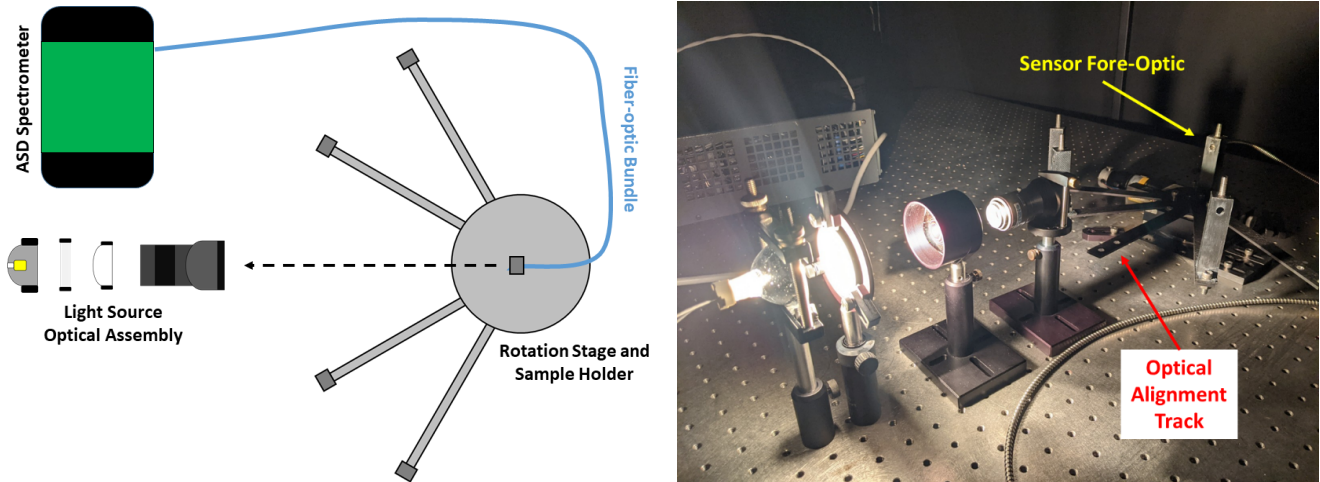


**Figure 3.** The goniometer system used in this study when measuring incident irradiance. (Left) A diagram of the major components showing the positioning of the spectrometer fore-optic facing the light source. (Right) An image of the setup when measuring the incident radiance onto the target plane.

the principal plane of scattering such that  $\phi_i = \phi_r = 0$ , so these terms are ignored for simplicity in the following equations. Also note that all radiometric terms in this section are wavelength dependent, but that the wavelength term  $\lambda$  is not written for simplicity.

### 2.2.1. Measurement of Incident Irradiance

The first term that must be measured is the incident irradiance onto the targeted plane,  $E_i(\theta_i)$ , in units of  $\text{Watts}/m^2$ . In order to measure the irradiance, the spectrometer system is set up such that the light source directly illuminates the spectrometer fore-optic at the sample target plane using an optical alignment track. A diagram of this system in this configuration is shown in Figure 3. It can be seen in this Figure that when measuring the incident beam power, the sensor fore-optic is aligned facing the light source. The system records spectral radiance measurements for a period of 60 seconds. The measurements are then averaged to produce the average spectral incident radiance at the nadir orientation,  $L_i(\theta_i = 0^\circ) = L_{i_0}$ .

The term  $L_{i_0}$  is measured in units of  $\text{Watts}/m^2/\text{sr}$ . In order to obtain the desired incident irradiance  $E_{i_0}$  in units of  $\text{Watts}/m^2$ , we must multiply  $L_{i_0}$  by the solid-angle subtended by the light source,  $\Omega_b$ . Our method for evaluation of the light source solid angle was derived and outlined in Appendix A and the determined value was used in our processing scheme. Using the derived solid angle of the

incident beam, the radiance is converted into irradiance according to:

$$E_{i_0} = L_{i_0} \times \Omega_b \quad (1)$$

In order to take into account projected area effects of the beam onto the sample when the planar sample is rotated, we multiply by a cosine factor (Budding & Demircan 2007). The general equation for incident irradiance onto the sample as a function of the angle between the incident light source direction and the sample normal direction,  $\theta_i$ , is then given by:

$$E_i(\theta_i) = E_{i_0} \times \cos(\theta_i) \quad (2)$$

The angle  $\theta_i$  can be measured to within  $0.5^\circ$  given the accuracy of the Newport optical rotation stage used in our setup.

### 2.2.2. Measuring Reflected Sample Radiance

The numerator of the BRCF equation is the reflected sample radiance into a direction of  $\theta_r$  due to irradiance from a light source oriented at direction  $\theta_i$ . Because the ASD FieldSpec 4 spectrometer measures the radiance in units of Watts/m<sup>2</sup>/sr directly, there is no need for a conversion of the sample radiance measurements.

The spectrometer system configuration for measuring received sample radiance is shown in Figure 4. When measuring received sample radiance, the sensor fore-optic is secured within machined fore-optic holders that precisely orient the spectrometer towards the center of the sample of interest. These slots are positioned approximately 7 inches away from the target center, resulting in a subtended viewing extent of 4.3 inches<sup>2</sup>. This viewing extent roughly matches the target area size of 4 inches<sup>2</sup>, which minimizes the amount of background scene that is incorporated into the sample radiance measurements. These machined holders are denoted in the right image of Figure 4 for all five  $\theta_r$  values used in our goniometer system:  $-60^\circ$ ,  $-30^\circ$ ,  $0^\circ$ ,  $30^\circ$ , and  $60^\circ$ .

### 2.2.3. Processing Empirical Measurements

In our processing codes, the measured sample radiance and incident light source irradiance are processed according to the incident beam direction,  $\theta_i$ , and exitant viewing direction,  $\theta_r$ . These terms are combined into the BCRF equation according to the following equation:

$$f_r(\theta_i, \theta_r) = \frac{L_r(\theta_i, \theta_r)}{L_{i_0} \Omega_b \cos \theta_r \cos \theta_i} \quad (3)$$

where  $L_r(\theta_i, \theta_r)$  is the measured sample radiance from a given viewing and illumination orientation, and  $\cos \theta_r$  accounts for the projection of the spectrometer's subtended solid angle onto the normal direction of the sample (Budding & Demircan 2007).

## 2.3. Photometric BRDF

In order to perform the model inversion within desired bandpasses of interest, we utilize the concept of a photometric BRDF. This concept allows us to understand how the spectral energy density of light reflected from the spacecraft materials behaves as the observational geometry is varied for bandpasses of interest to the user. This idea is similar to the concept of *spectral BRDF* that has been defined by other researchers in the community (Bedard et al. 2011; Bédard et al. 2015).

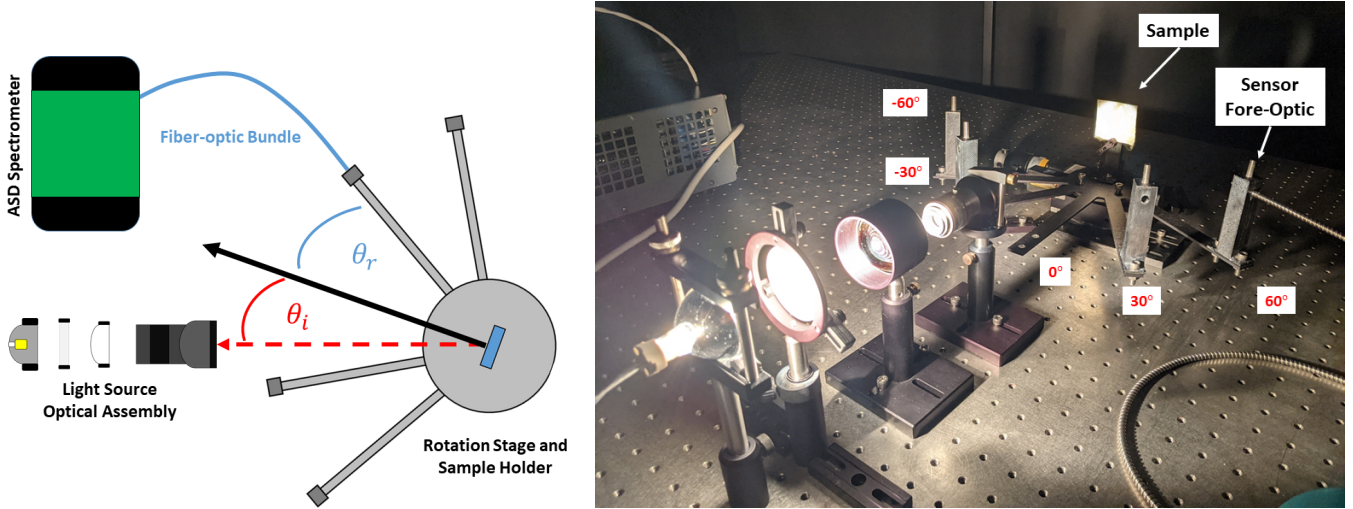


**Figure 4.** The goniometer system used in this study when measuring a sample. (Left) A diagram showing the main components of the system and the conventions for the viewing orientation ( $\theta_r$ ) and illumination orientation ( $\theta_i$ ). (Right) A figure of the system when measuring a sample with the location of the fiber optic at the  $\theta_r = +60^\circ$  location, and the fiber optic holder slots labeled by  $\theta_r$  value.

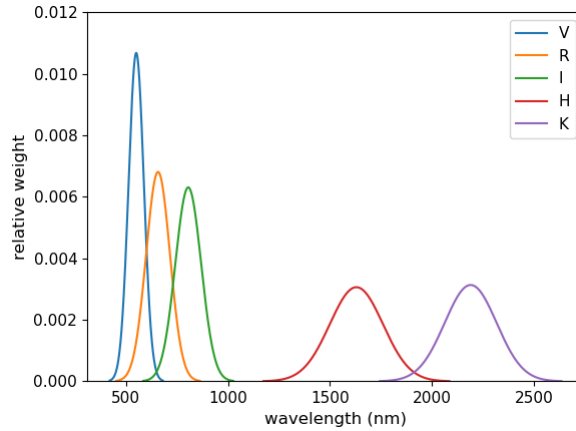


**Figure 5.** The photometric filters,  $P(\lambda)$ , used in the BRDF model inversion in this study. The legend denotes the corresponding filter label for a given color code (Budding & Demircan 2007)

The definition of the photometric BRDF can be given by:

$$f_P(\theta_i, \theta_r) = \sum_{\lambda_{P,l}}^{\lambda_{P,u}} P(\lambda) \frac{L_r(\theta_i, \theta_r, \lambda)}{L_{i_0}(\lambda) \Omega_b \cos \theta_r \cos \theta_i} \quad (4)$$

where  $P(\lambda)$  is the normalized filter weight value for the bandpass of interest at wavelength  $\lambda$ , and  $\lambda_{P,l}$  and  $\lambda_{P,u}$  are the lower and upper bounds of this bandpass, respectively. The bandpasses chosen for this study are from the photometric system and are shown in Figure 5

### 3. BRDF MODEL INVERSION

In this study, the Ward BRDF model was utilized in the inversion routine on the empirical measurements (Ward 1992). The Ward BRDF model was developed for the computer graphics community as

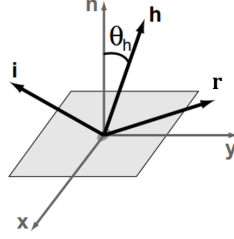


**Figure 6.** Coordinate conventions used in the Ward BRDF model. The z-axis is defined as the surface normal  $\mathbf{n}$ , with the x- and y-axes along the surface’s tangent plane. The half direction  $\mathbf{h}$  is defined to lie midway between the incident light direction,  $\mathbf{i}$ , and the exitant viewing direction,  $\mathbf{r}$  (Walter 2005).

an alternative to popular models which could violate the laws of physics (Walter 2005). For example, certain combinations of parameters used in the Phong BRDF model may not conserve energy by reflecting more energy that is incident onto the target (Ngan et al. 2005). The goal of the model was to develop a mathematical representation that (1) is physically valid and (2) fits empirical BRDF datasets (Ward 1992). Importantly, this model is a component of the Digital Imaging and Remote Sensing Image Generation (DIRSIG) radiometric modeling tool employed in this study to simulate radiometric modeling of satellites of interest (Goodenough & Brown 2012).

### 3.1. Ward BRDF Model

The geometry of the Ward BRDF model is heavily based on the concept of the half direction  $\mathbf{h}$  that is defined to be halfway between the illumination and viewing directions. It can be computed by adding  $\mathbf{i}$  and  $\mathbf{r}$  as 3D vectors and then re-normalizing, as can be shown in the following equation and in the diagram in Figure 6:

$$\mathbf{h} = \frac{\mathbf{i} + \mathbf{r}}{\|\mathbf{i} + \mathbf{r}\|} \quad (5)$$

The half direction can then be expressed in spherical coordinates according to the conversion  $\mathbf{h} = [\sin \theta_h \cos \phi_h, \sin \theta_h \sin \phi_h, \cos \theta_h]$ , where  $\theta_h$  is the zenith component and  $\phi_h$  is the azimuth component. Ward specifies that the BRDF model can be expressed in spherical coordinates for a more exact, but computationally expensive form (Ward 1992).

Using this geometry, the Ward BRDF model can be defined as the sum of two components: a diffuse (or Lambertian) term, and a specular term (Ward 1992). The equation utilized in our inversions is given by the following form:

$$f_{ward}(\theta_i, \phi_i; \theta_r, \phi_r) = \frac{\rho_d}{\pi} + \frac{\rho_s}{4\pi\alpha_x\alpha_y\sqrt{\cos\theta_i\cos\theta_r}} e^{-\tan^2\theta_h\left(\frac{\cos^2\phi_h}{\alpha_x^2} + \frac{\sin^2\phi_h}{\alpha_y^2}\right)} \quad (6)$$

where where  $\rho_s$  controls the magnitude of the specular reflectance,  $\alpha_x$  and  $\alpha_y$  specify the width of the specular lobe in the two principal directions of anisotropy from Figure 6, and  $\rho_d$  is the Lambertian reflectance term that is not dependent on viewing or illumination direction. These four parameters fully control the way that light is scattered into a hemisphere above a target and are the parameters for which we invert the model for each material sample.

It should be noted that while the Ward BRDF model is able to adequately model the forward scattering of light and the anisotropy of light, the ability to model back-scattering is limited. Most

spacecraft materials utilized in this study did not exhibit significant backscattering, so it was not a concern for our purposes of demonstrating our radiometric modeling pipeline. However, we plan on addressing this limitation in future modeling efforts.

### 3.2. Model Inversion Routine

For each set of measurements, we seek to invert the theoretical Ward BRDF model to the collected BCRF measurements in Equation 6. The 4-dimensional parameter vector that we solve for is denoted by  $\Theta_{\mathbf{W}} = (\rho_d, \rho_s, \alpha_x, \alpha_y)$ . In order to solve for the optimal parameters, we employ a two-step inversion algorithm similar to the one employed by Badura et al. (2020). In the first step, initial estimates for  $\Theta_{\mathbf{W}}$  are found using an evolutionary algorithm. In the second step, the initial estimates are then fed into a non-linear least squares descent routine to find the global optimum solution. Conjugate-gradient descent methods are notoriously sensitive to initial parameter estimates, so this two-step approach mitigates the potential of getting trapped in a local optimum solution.

The evolutionary algorithm used to determine initial estimates for each of the BRDF parameters was the Particle Swarm Optimization (PSO) algorithm. Search particles are randomly distributed within the parameter space and allowed to travel iteratively towards their local optimal solution, while being influenced by the best global solution of all particles. In this way, the trajectory of particles within the parameter space is influenced by both individual search behavior and collective group action (Shi & Eberhart 1998). The implementation of PSO chosen for this work was the PySwarms python module (Miranda et al. 2018). Experimentation revealed that good convergence across randomly seeded runs was achieved when using a 1000 particle swarm with cognitive parameter of 0.5, social parameter of 0.3, and weight parameter of 0.9.

The results of the optimal solution found by the PSO optimizer are used as initial parameter estimates for a conjugate gradient descent routine. The PSO algorithm does not compute a numerical gradient when updating the velocities of individual particles (Shi & Eberhart 1998). PSO therefore requires the best estimate to be fed into a gradient descent routine in order to determine the true global optimal solution. In this study, the Levenberg-Marquardt algorithm was utilized, with the Jacobian of each of the search parameters given by Equation 7 (Moré 1978):

$$J_{ward} = \begin{bmatrix} \frac{\partial f_{ward}}{\partial \rho_d} \\ \frac{\partial f_{ward}}{\partial \rho_s} \\ \frac{\partial f_{ward}}{\partial \alpha_x} \\ \frac{\partial f_{ward}}{\partial \alpha_y} \end{bmatrix} = \begin{bmatrix} 1/\pi \\ \frac{1}{4\pi\alpha_x\alpha_y\sqrt{\cos\theta_i\cos\theta_r}} e^{-\tan^2\theta_h\left(\frac{\cos^2\phi_h}{\alpha_x^2} + \frac{\sin^2\phi_h}{\alpha_y^2}\right)} \\ \frac{\rho_s}{4\pi\alpha_x^2\alpha_y\sqrt{\cos\theta_i\cos\theta_r}} \left[ \frac{2\tan^2\theta_h\cos^2\phi_h}{\alpha_x^2} - 1 \right] e^{-\tan^2\theta_h\left(\frac{\cos^2\phi_h}{\alpha_x^2} + \frac{\sin^2\phi_h}{\alpha_x^2}\right)} \\ \frac{\rho_s}{4\pi\alpha_y^2\alpha_x\sqrt{\cos\theta_i\cos\theta_r}} \left[ \frac{2\tan^2\theta_h\sin^2\phi_h}{\alpha_y^2} - 1 \right] e^{-\tan^2\theta_h\left(\frac{\cos^2\phi_h}{\alpha_x^2} + \frac{\sin^2\phi_h}{\alpha_y^2}\right)} \end{bmatrix} \quad (7)$$

The global optimum solution is defined as the point in the 4-dimensional parameter space  $\Theta_{\mathbf{W}}$  at which the residual function between the modeled BRDF function and the empirical BRDF measurements is at a minimum. The residual function used in the inversion routine is defined for a photometric bandpass filter  $P$  as:

$$C_P(\Theta_{\mathbf{W}}) = \sum_{y=0}^{N_m} [f_P(\theta_{i_y}; \theta_{r_y}) - f_{ward}(\Theta_{\mathbf{W}}; \theta_{i_y}; \theta_{r_y})]^2 \quad (8)$$

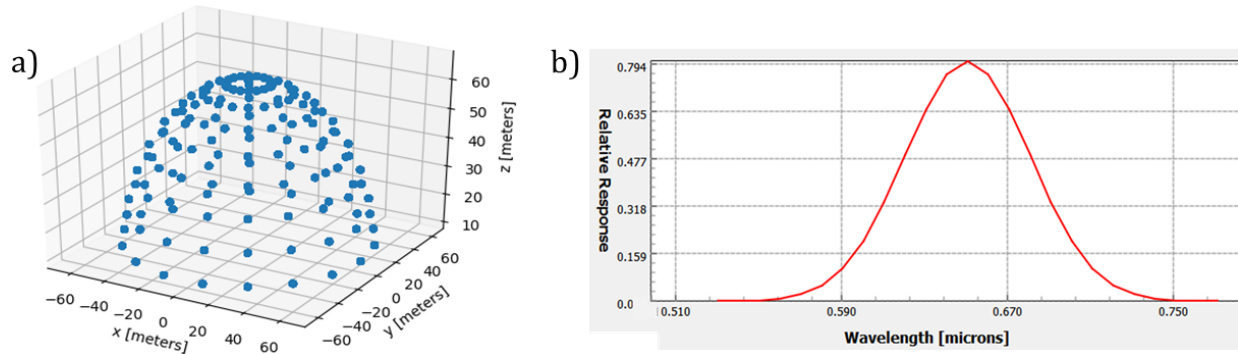


**Figure 7.** The design of a synthetic spectrometer for modeling sub-pixel BRDF mixing: (a) a hemispherical scan pattern used for our synthetic spectrometer to measure a  $1 \text{ m}^2$  RSO face, and (b) the spectral bandpass of the synthetic spectrometer used to model the R-band of the photometric system from Figure 5.

where  $N_m$  is the number of combinations of multi-angle spectral observation angles,  $f_P$  is the empirical photometric BRDF measurement for filter  $P$  with illumination orientation  $\theta_{i_y}$  and viewing orientation  $\theta_{r_y}$ , and  $f_{ward}(\Theta_{\mathbf{w}}; \theta_{i_y}; \theta_{r_y})$  is the value of the Ward BRDF function at the view-illumination geometry corresponding to the experimental measurement.

The metric of evaluation utilized to determine the accuracy of the fitting routine is given by the equation of the root mean square error,  $RMSE = \sqrt{C_P(\Theta_{\mathbf{w}})/N_m}$ . This metric is frequently used in studies for fitting empirical BRDF data to theoretical BRDF models (Li & Strahler 1992; Badura et al. 2020). The optimal set of parameters was found for each of the filters shown in Figure 5.

#### 4. RADIOMETRIC MODELING & SIMULATION

The DIRSIG model has been actively developed at the Digital Imaging and Remote Sensing (DIRS) Laboratory at Rochester Institute of Technology (RIT) for two decades. The model is designed to generate passive broadband, multi-spectral and low-light imagery using a suite of first-principles based radiation propagation modules (Ientilucci & Brown 2003; Schott et al. 1999). The code allows for the specification of payload, optical instrument, and RSO reflectance properties in order to model a desired scene of interest. The code has seen recent advances and interest in the SDA community for the purposes of modeling radiometrically accurate RSO signatures (Bennett et al. 2014). In this study, tools were developed in order to ingest the inverted BRDF datasets from this study and another recent study by Badura et al. (2020) in order to simulate (1) unresolved BRDF mixing of different materials, and (2) resolved space-to-space imagery of RSO's using standard RGB sensors.

##### 4.1. Modeling Unresolved Mixing of Materials

There are three main components that we use to simulate sub-pixel mixing of BRDF signatures of materials due to factors such as multiple-scattering, self-shadowing, obscuration, and sensor geometry effects. These include (1) the atmospheric illumination onto the target, (2) the field of view of the spectrometer, and (3) the spectral bandpass of interest. A brief overview of a few of the input spectrometer design parameters is shown in Figure 7 and discussed below.

###### 4.1.1. Collimated Light

DIRSIG allows the user to tailor the incident hemispherical irradiance and direct radiance reaching the target of interest. This concept is used to generate a scene setup that can be utilized to directly

generate BRDF measurements. For reference, the differential form of BRDF can be written in the following manner:

$$\partial f_{BRDF}(\theta_i, \phi_i; \theta_r, \phi_r) = \frac{\partial L_r(\theta_i, \phi_i; \theta_r, \phi_r)}{E'_i(\theta_i, \phi_i) \cos \theta_i} \quad (9)$$

where  $\partial L_r$  is the received radiance within an integrable solid angle,  $E'_i$  is the incident irradiance onto the target, and the terms  $\phi_i$  and  $\phi_r$  denote the incident and receiver azimuth locations, respectively.

The term  $E'_i$  can be modeled in DIRSIG using a “uniform” atmospheric model. This model divides the light from the atmosphere into two components: (1) uniform hemispherical irradiance and (2) direct radiance from a sun-sized source. The sun sized source provides collimated light onto the target, and is the primary component of interest to the BRDF measurements. Therefore, the hemispherical irradiance component is set to zero in our simulations. Within this convention, we simply need to specify the magnitude of the direct radiance term  $E_i$  in units of Watts/m<sup>2</sup>. By setting this value equal to  $E'_i = 1/\cos \theta_i$ , the equation for DIRSIG’s measured value becomes:

$$\partial f_{BRDF}(\theta_i, \phi_i; \theta_r, \phi_r) = \frac{\partial L_r(\theta_i, \phi_i; \theta_r, \phi_r)}{\left(\frac{1}{\cos \theta_i}\right) \cos \theta_i} = L_r(\theta_i, \phi_i; \theta_r, \phi_r) \quad (10)$$

In other words, DIRSIG is able to provide a scaled form of the BRDF directly to the user by using this “trick” for setting up parameters. By specifying the bandpass of interest and the target’s BRDF properties within the bandpass of interest, the user can directly obtain the unresolved BRDF signature that would be observed by a sensor.

#### 4.1.2. Simulated Goniometer

DIRSIG allows the user to create a spectrometer that mimics the finite spectrometer field of view utilized in our laboratory setup from Figure 4. In order to achieve this, there are two tradeoffs that we consider in our spectrometer design, as specified by past DIRSIG studies ([Ientilucci & Brown 2003](#)):

1. **Constant Angle of Collimated Light** - For a given viewing orientation of the spectrometer, all sampled photons should be measured from approximately the same angle relative to the RSO’s average normal direction.
2. **Constant Area of the Target Face Visible** - Regardless of the viewing angle, the total area of the RSO face visible by the spectrometer scene should be constant.

Typical sensors created in the DIRSIG simulation tool and in real-world experimental setups will violate both of these constraints. Therefore, we create some tradeoffs in our design formulation in order create a realistic sensor paradigm for approximating BRDF using the BCRF convention from Figure 1 (b).

For constraint #1, it should be noted that at close distances to the RSO face, the field of view of the fore-optic (i.e. the value  $\Omega_{fo}$  in Figure 1 (b)) will naturally introduce angular variation due to allowing photons from a variety of directions into the receiver. For the case of DIRSIG simulations, because we are tracing photons in an atmosphere with 100% transmittance and therefore have no concerns about signal-to-noise, this problem can be overcome by simply placing the sensor at a

very far distance from the RSO face being measured. In other words, by placing the fore-optic at a distance many times the extent of RSO’s projected area, the allowed range of incident photon normal directions allowed to hit the receiver shrinks. For our case, we are simulating a target 1 m<sup>2</sup> in extent, so we place our target at a distance of 65 m away from the target. An example scan pattern for measuring an RSO of this size is shown in Figure 7 (a).

For constraint #2, we seek to overcome this issue by maintaining the same area on the RSO face for all viewing zenith orientations,  $\theta_r$ . One way to overcome this is by dynamically changing the field of view of the sensor to exactly match the projected area of the RSO face scaled by the  $1/\cos \theta_r$  projected area factor. A second way to overcome this is by simply sampling a much larger extent than the RSO face, but only accepting photons from the RSO face. We choose to utilize this second method in DIRSIG by placing an absorber far below the RSO face being measured that has 100% absorbance and 0% transmittance. In this way, it captures all photons that do not hit the target but allows photons from the RSO face to be measured by the synthetic spectrometer.

#### 4.1.3. *Sensor Bandpass*

In order to model the spectrometer bandpass of interest for a given photometric filter, DIRSIG allows the user to specify (1) the BRDF of a material within a given sensor bandpass and (2) the spectrometer bandpass. DIRSIG can ingest and model multiple photometric filters at the same time, as will be shown in the next section when producing radiometrically-realistic RGB imagery. For the purposes of modeling sub-pixel BRDF mixing within a bandpass of interest, we utilize photometric filters, with the modeled R-band in DIRSIG’s graphical-user-interface being shown in Figure 7 (b).

#### 4.2. *Modeling Resolved Color Imagery*

Modeling resolved RGB imagery in the DIRSIG environment is simpler to implement than the synthetic goniometer system. DIRSIG ingests two-line-element (TLE) datasets that allow the user to specify the position of an RSO and the position of the illumination source over time. DIRSIG further allows for the user to specify the time-dependent maneuver properties of the RSO under study. For example, in this paper we simulate an uncontrolled RSO that is tumbling while being imaged by our sensor payload. DIRSIG also allows the user to specify red, green, and blue color channels for the sensor as opposed to the photometric channels from Figure 5. In addition, the BRDF inversion data can be ingested for each channel and spectrally interpolated at in-between wavelengths. All of these concepts are utilized in the presented simulation in this paper, and can be extended in future studies.

### 5. RESULTS

#### 5.1. *BCRF Measurement Results*

BCRF measurements of 20 pristine samples were obtained using the experimental setup and processing pipeline outlined in Section 2. Images of 15 samples and their names are shown in Figure 8. The 15 shown materials in Figure 8 will be also used in the Materials International Space Station Experiment (MISSE) in early 2022. The remaining 5 samples of the 20 total samples were measured for the relevance to the SDA community.

Spectral directional reflectance data is presented in this section to illustrate the wavelength-dependent nature of BCRF measurements. For the sake of focus on the modeling and simulation,

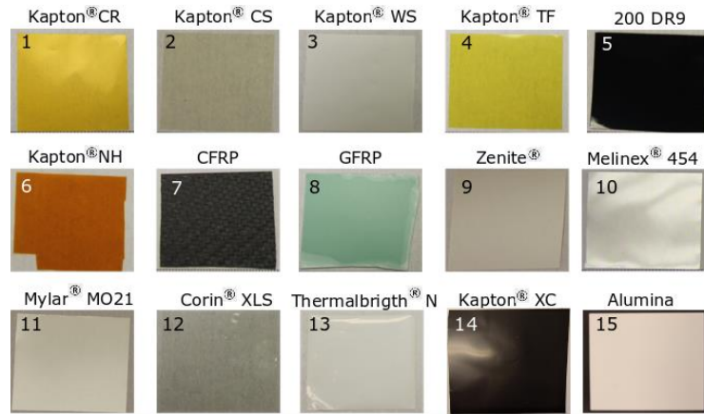


**Figure 8.** The samples measured using the goniometer system in this study

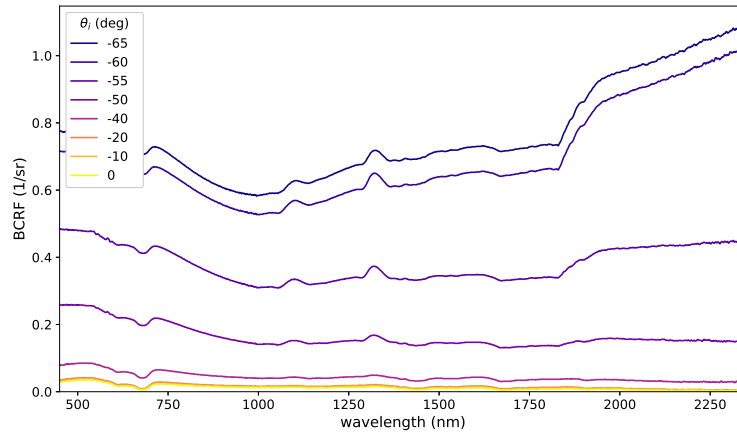


**Figure 9.** BCRF Measurement of the GFRP sample for viewing orientation of  $\theta_r = 60^\circ$

just a few of the samples will be assessed and discussed in this paper that are representative of the properties observed for the various samples.

#### 5.1.1. Glass Fiber Reinforced Polymer (GFRP) Sample

A subset of BCRF measurements for GFRP (sample # 8 in Figure 8) obtained at a receiver viewing orientation of  $\theta_r = 60^\circ$  is shown in Figure 9. The sample is a relatively diffuse reflector, and not very transmissive. Several observations can be made about this sample from the measurements.

From Figure 9, it can be seen that the sample has a forward scattering lobe that is stronger in the direction of  $\theta_i = -65^\circ$  than in the specular direction of  $\theta_i = -60^\circ$ . It can also be seen that the magnitude of the BCRF decreases over the spectral range of 500-1000 nm and then increases over the range of 1750-2300 nm. This spectral dependence is most noticeable near the specular direction.

#### 5.1.2. Kapton NH Sample

Measurements of Kapton NH (sample # 6 in Figure 8) for viewing orientations of  $\theta_r = 30^\circ$  and  $\theta_r = 60^\circ$  can be seen in Figure 10. Note that there appear to be interpolation artifacts resulting from the spectrometer processing software bridging the spectral measurements across the different sensors

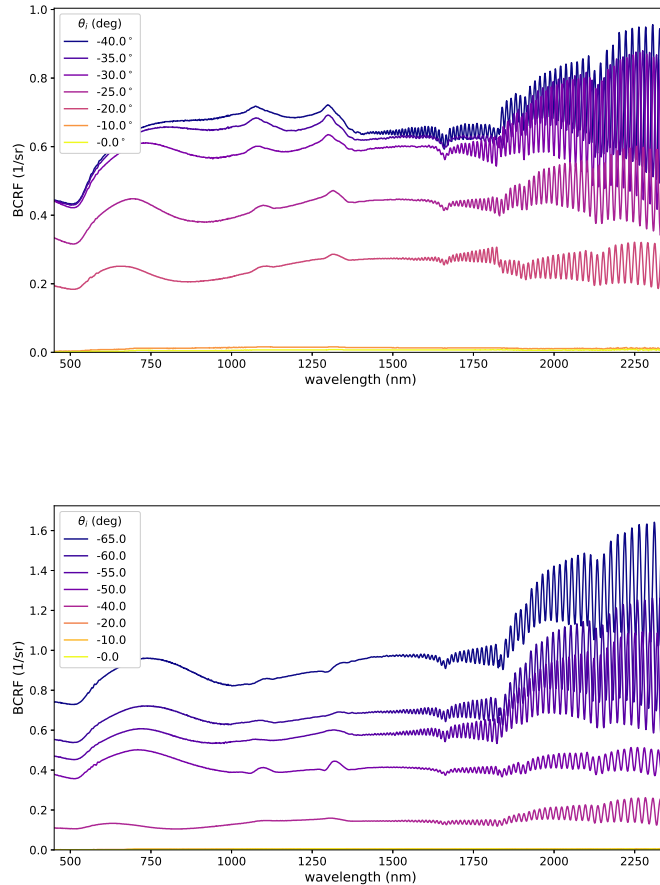


**Figure 10.** BCRF measurements of Kapton NH for a viewing orientation of  $\theta_r = 30^\circ$  (top) and  $\theta_r = 60^\circ$  (bottom).

of the ASD FieldSpec 4 at approximately 1200 nm and 1800 nm. This behaviour showed up in several measurements and is likely due to the proprietary software used to post-process the radiance measurement files.

A few interesting things can be discerned from the raw spectral BCRF measurements. The most notable is that there is an interference pattern that appears above wavelengths of approximately 1600 nm. The material Kapton NH is composed of multiple thin films, which causes multi-layer reflections that manifest themselves as interference patterns. This type of phenomena has been observed in other studies on spacecraft thin film BRDFs (Bédard et al. 2015). We are actively investigating methods for processing this data in order to preserve the spectral trend while minimizing the presence of the interference.

Another interesting observation from the BCRF measurements in Figure 10 is that the magnitude of the BCRF is relatively constant as a function of wavelength. There do appear to be slight increases in BCRF magnitude around the wavelengths of 750 nm and 2100 nm, but the relative spectral trend is otherwise flat, suggesting that Kapton NH has a relatively wavelength-independent BCRF in the principal plane of scattering.

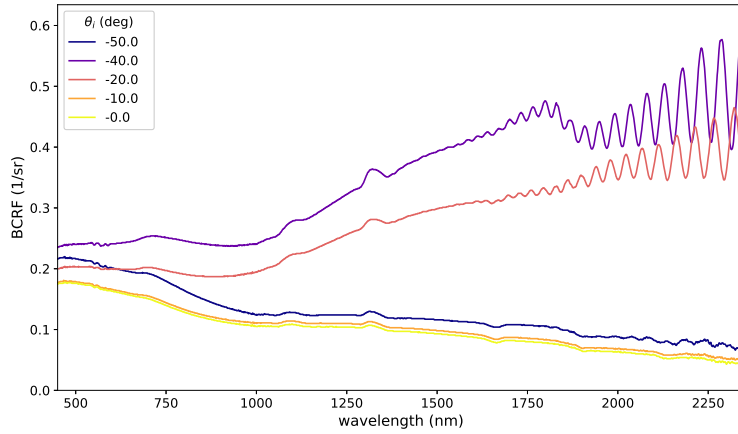


**Figure 11.** BCRF Measurement of the Kapton WS Gloss 1 mm sample for viewing orientation of  $\theta_r = 30^\circ$

It can also be discerned that the magnitude of the specular lobe of the BCRF only marginally increases by approximately 25% as the viewing orientation goes from  $\theta_r = 30^\circ$  to  $\theta_r = 60^\circ$ . The material does not appear to be a perfect specular scatterer, as the greatest BCRF magnitudes occur at illumination orientation  $\theta_i = -40^\circ$  for viewing orientation  $\theta_r = 30^\circ$ , and at illumination orientation  $\theta_i = -65^\circ$  for viewing orientation  $\theta_r = 60^\circ$ . Because the BRDF of a material satisfies Helmholtz reciprocity such that  $f_{BRDF}(\theta_i, \phi_i; \theta_r, \phi_r) = f_{BRDF}(\theta_r, \phi_r; \theta_i, \phi_i)$ , this behavior means that the material is potentially a forward scattering material rather than a mirror-like material (Li et al. 2006).

It can also be noted that the material Kapton NH is almost completely transparent at nadir illumination orientations and off-nadir viewing orientations in Figure 10. The material is nearly completely opaque around the specular and forward-scattering directions.

### 5.1.3. Kapton WS Gloss Sample

The Kapton WS Gloss (sample # 3 in Figure 8) sample BCRF measurement for a viewing orientation of  $\theta_r = 30^\circ$  is shown in Figure 11.

This sample exhibits very unique spectral behavior as the incident light orientation changes. For illumination orientations that we measured that were not near the back-scattering direction (i.e.  $\theta_i \in [0^\circ, -10^\circ, -50^\circ]$ ), the sample has a consistently decreasing BCRF as a function of wavelength. However, when the illumination orientation was in the back-scattering direction (i.e.  $\theta_i \in [-20^\circ, -40^\circ]$ ), the BCRF steadily increased as a function of wavelength.

Another thing to note is that this sample exhibited interference for the forward scattering illumination orientations above the wavelength of 1800 nm. This is likely due to the fact that this sample was also composed of multiple thin films.

### 5.1.4. Thermbright Sample

Measurements of Thermbright (sample # 13 in Figure 8) for the viewing orientation of  $\theta_r = 60^\circ$  can be seen in Figure 12. This sample is a relatively diffuse white reflector that exhibits a strong forward scattering behavior.

From the plots in Figure 12, we can see that there is a very gradual rise in BCRF as the illumination orientation goes from the nadir illumination orientation of  $\theta_i = 0^\circ$  to the oblique illumination direction

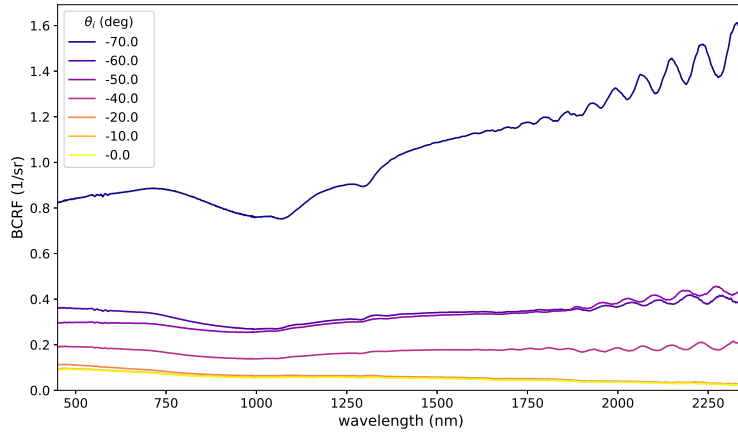


**Figure 12.** BCRF Measurement of the Thermbright sample for viewing orientation of  $\theta_r = 60^\circ$

of  $\theta_i = -60^\circ$ . The BCRF is also relatively constant as a function of wavelength for all of these illumination orientations.

The sample deviates from this behavior in that it has a very strong forward scattering BCRF for the extreme oblique illumination orientation of  $\theta_i = -70^\circ$ . The magnitude of the BCRF at this illumination orientation is nearly three times stronger than the specular BCRF measurement obtained when the light source was at an orientation of  $\theta_i = -60^\circ$ . In addition, the BCRF steadily increases as a function of wavelength for the illumination orientation of  $\theta_i = -70^\circ$  and viewing orientation of  $\theta_r = +60^\circ$ , which deviates from smooth spectral behavior observed at the other illumination orientations.

Once again, we note that this sample is composed of multiple thin films. This leads to the interference pattern that is observed for forward scattering illumination orientations at wavelengths above 1800 nm.

## 5.2. Photometric BRDF Inversion

In this section, we present the inversion results that were obtained using the procedure outlined in Section 3.2. The empirical data from the photometric BCRF definition in Equation 4 was fit to the theoretical Ward BRDF model given by Equation 6. The optimal solution for this fit was defined using the RMSE equation from Equation 8 on a per-bandpass basis. Only a few of the material results are discussed and presented for the sake of focus on the overall trends found in our results.

### 5.2.1. Kevlar Inversion Results

The results of the inversion procedure for the photometric BRDF measurements of a Kevlar fabric sample (not shown in Figure 8) are shown in Figure 13 for an illumination orientation of  $\theta_i = -20^\circ$ . The material is a fairly strong forward scattering material.

The empirical measurements that have been quadratically interpolated to 10 degree increments are shown as scatter plot points. The empirical measurements show that there is a slight back-scatter lobe that peaks around  $\theta_r = -50^\circ$ . The empirical measurements also show that the Kevlar fabric is not a perfect specular scatterer, given that the specular direction occurs at  $\theta_r = 20^\circ$  and the empirical measurements peak around approximately  $\theta_r = 40^\circ$ .

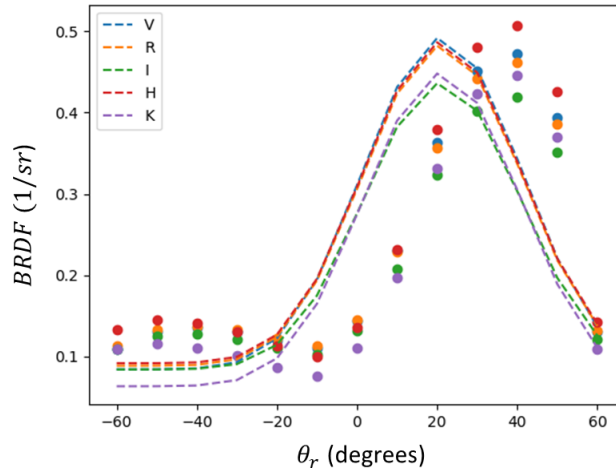


**Figure 13.** The fitted empirical BRDF data (dashed lines) and the interpolated empirical BCRF data (circle scatter plot) for the Kevlar sample for a fixed illumination orientation of  $\theta_i = -20^\circ$  as the viewing orientation changes.

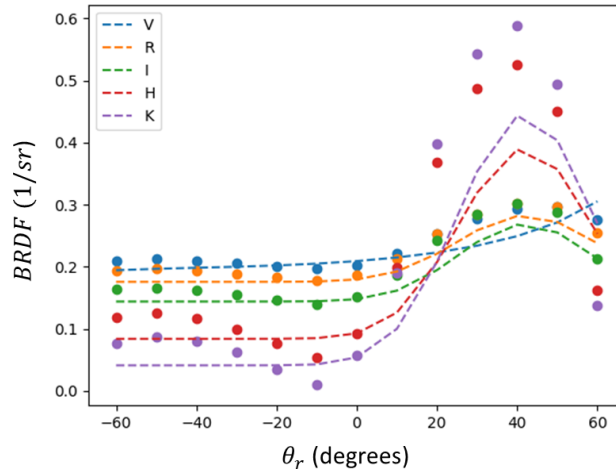


**Figure 14.** The fitted empirical BRDF data (dashed lines) and the interpolated empirical BCRF data (circle scatter plot) for the Kapton WS Gloss sample for an illumination orientation of  $\theta_i = -40^\circ$ .

The optimal Ward parameters predict that the material has no back-scattering lobe, and that the material has a wide specular lobe centered at  $\theta_r = +20^\circ$ . These limitations show that a more complex model such as the Beard-Maxwell model may be required to properly describe the BRDF properties of many spacecraft materials (Badura et al. 2020). The focus in this study, however, was on outlining a procedure to take laboratory measurements into a modeling and simulation environment. In future studies, this can be corrected by using a goniometer that can sample the hemisphere of scattering more finely and by fitting the data to a more complex theoretical BRDF model.

### 5.2.2. Kapton WS Gloss Inversion Results

The results of the inversion procedure for the Kapton WS Gloss sample are shown in Figure 14 for an incident illumination angle of  $\theta_i = -40^\circ$ . The fit results indicate that the material is approximately Lambertian in the  $I$ ,  $R$ , and  $V$  bands, while the sample is specular in the  $H$  and  $K$  bands.

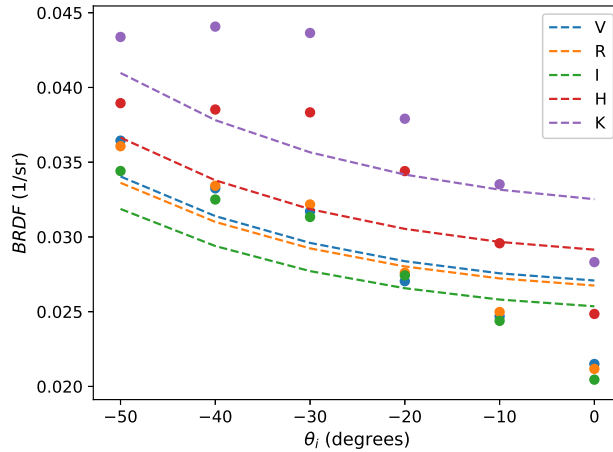


**Figure 15.** The fitted empirical BRDF data (dashed lines) and the interpolated empirical BCRF data (circle scatter plot) for the CFRP sample for a fixed viewing orientation of  $\theta_r = +30^\circ$  as the illumination orientation changes.

Overall, the fit between the quadratically interpolated empirical data and the theoretical model follow the same trend for the  $H$  and  $K$  bands. The optimal parameters for the Ward BRDF model when integrated over the  $H$  and  $K$  photometric bands under-predict the interpolated empirical specular BRDF magnitude by almost 33%. This could potentially be due to the slight back-scatter lobe that shows up in the data for the  $H$  and  $K$  empirical BRDF data. The Ward model is not able to adequately model this back-scatter lobe, indicating that a more complex BRDF model is necessary for simulating this material’s reflectance properties in the  $H$  and  $K$  bands.

The model is able to adequately describe the scattering behavior of the WS Gloss sample for the  $V$ ,  $R$ , and  $I$  bands. This is likely due to the fact that the photometric BRDF of Kevlar over these bands is approximately Lambertian, with a small forward scattering lobe.

### 5.2.3. CFRP Inversion Results

The results of the inversion procedure for the photometric BRDF measurements of the CFRP sample are shown in Figure 15 for a receiver orientation of  $\theta_r = +30^\circ$ . The fit results indicate that the material is fairly Lambertian across all bands.

The sample, however, does have a persistent back-scatter lobe that shows up in the range of incident illumination orientations of -30 to -50 degrees. The Ward BRDF model is not able to adequately model this phenomena, meaning that more complex models are required to describe this material’s scattering behaviors.

## 5.3. Radiometric Modeling and Simulation

### 5.3.1. Simulated BRDF Results

For the case of simulating unresolved material mixing that was described in Section 4.1, we created 1  $m^2$  target that was comprised of four different 0.5  $m^2$  panels of different materials: Thermbright, Kapton CS, CFRP and WS-Gloss. Two different scenarios were used in order to model multiple-scattering effects on unresolved BRDF signatures of the material surface. In the first scenario, the panels were all completely flat, as can be seen in Figure 16 (a). In the second scenario, the panels

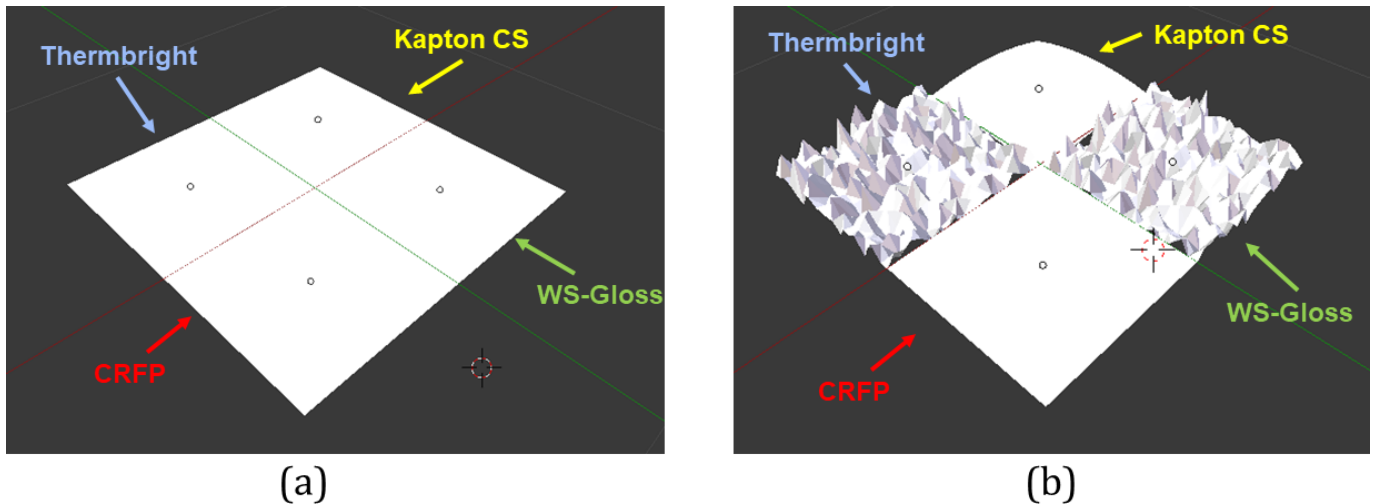


**Figure 16.** The samples used for demonstration of BRDF analysis. Each sample was attributed its Ward BRDF properties for the  $R$  band fit.

were bent and/or crinkled in order to create effects of shadowing and obscuration in the unresolved BRDF measurement. The samples were assigned the optimal Ward BRDF parameters for the  $R$  band resulting from the photometric BRDF inversion. The spectrometer was assigned an  $R$  band photometric filter and was positioned at each of the viewing geometries shown in Figure 7 (a) for a variety of illumination orientations.

The resulting BRDF measurement for an illumination orientation of azimuth angle  $\phi_s = 90^\circ$  and zenith angle  $\theta_s = 40^\circ$  are shown in Figure 17. The resultant BRDF of the flat panels from Figure 16 (a) is shown in Figure 17 (a), while the BRDF of the warped and crinkled panels from Figure 16 (b) is shown in Figure 17 (b).

This was mostly meant to be a theoretical example showing how one can model the effects of material mixing in unresolved BRDF signatures. However, there are several interesting things of note that can be observed from these polar renderings.

For the BRDF rendering of the smooth material sample in Figure 17 (a), we see that the widths forward and backward scattering lobes are equal in extent and relatively small at approximately  $30^\circ$  in angular width. It can also be seen that the forward scattering reflectance is strongest in magnitude in the range of zenith angles of  $+20^\circ$  to  $+40^\circ$  before rapidly falling off.

For the BRDF rendering of the textured material samples in Figure 17 (b), we see that DIRSIG predicts that the forward scattering lobe widens by approximately  $20^\circ$ . We also see that the strongest BRDF magnitude occur at extreme zenith angles of  $70^\circ$ , which deviates from the mirror-like behavior of the smooth sample. In addition, the overall BRDF magnitude has dropped by approximately 10% for all viewing angles. This result shows how the effects of multiple-scattering, facet self-shadowing, and viewer obscuration can lead to complex BRDF signatures that might not be capable of being modeled by a single theoretical BRDF model.

While the example shown in this paper is simply a thought experiment, this approach can be extended to modeling BRDFs of satellite faces in order to better approximate the BRDFs of satellites that may be comprised of convex geometries and multiple materials of varying spectral reflectance characteristics. Several previous studies have derived inversion methods based on models that (1) assume a singular BRDF for the satellite under study or (2) ignore the effects of multiple scattering

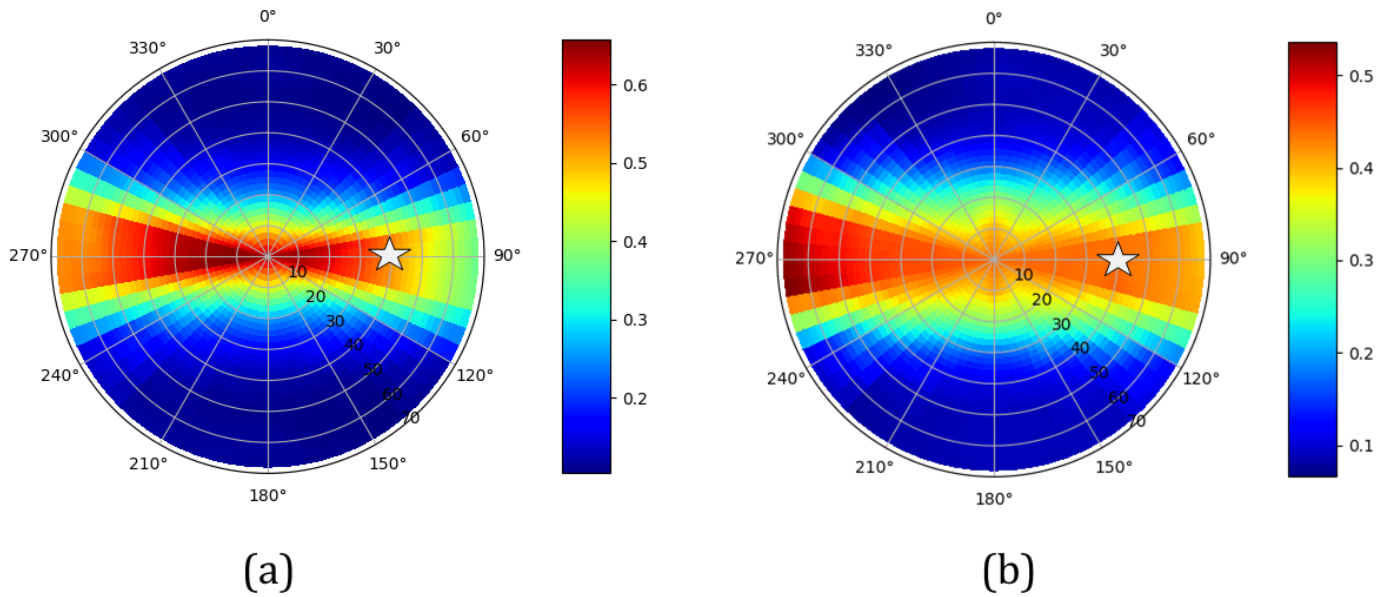


**Figure 17.** The resulting DIRSIG simulated BRDF over the hemisphere above the target’s normal direction. The incident illumination orientation is denoted by the white star at azimuth of  $90^\circ$  and zenith of  $40^\circ$ .

(Furfaro et al. 2018; Badura et al. 2020; Dianetti & Crassidis 2018). Our results provide a path towards deriving better approximations of satellite BRDF properties that can be used to simulate light curves based on better modeling of shadowing and multiple-scattering.

### 5.3.2. Space-to-Space Imaging Simulations

Using the approach described in Section 4.2, we simulated several images of 2U Cubesats and arbitrary satellites. The surfaces of the satellites were textured with the fitted BRDF properties in the red, green, and blue channels of several materials measured in this study such as Thermbright, Aluminized Kapton, and Kapton CS. In addition, several BRDF parameters from previous studies on silicon solar panels and gold antennae were utilized to simulate these materials based on the Beard-Maxwell BRDF model (Badura et al. 2020). The camera system was attributed with Gaussian photometric bandpasses in the red, green, and blue channels that integrated the radiance that reached each pixel on the focal plane array.

It should be noted that even though the user defines parameters such as the focal length, pixel pitches and relative spectral and spatial responses, DIRSIG 4 (which was used in this study) outputs aperture reaching radiance, leaving it to the user to simulate the camera properties beyond the light that hits the aperture. DIRSIG uses the camera parameter information to project the focal plane array onto the aperture and the radiance values reflect the radiance at that point in the optical path. In order to simulate the imaging chain past the aperture reaching radiance, we wrote code to convert the radiance into a digital count image based upon previous work in digital camera simulation (Farrell et al. 2012).

Using this method, several images of a 2U cubesat were rendered as it rotated about its center. Two such images are shown in Figures 18 and 19. In Figure 18, it can be seen that the antennae are barely visible in the imagery due to the lack of a strong specular reflection towards the camera. On the other hand, there is a strong glint coming from the Aluminized Kapton coating and the glass-coated silicon solar panels. For a second pose shown in Figure 19, there is a strong glint off

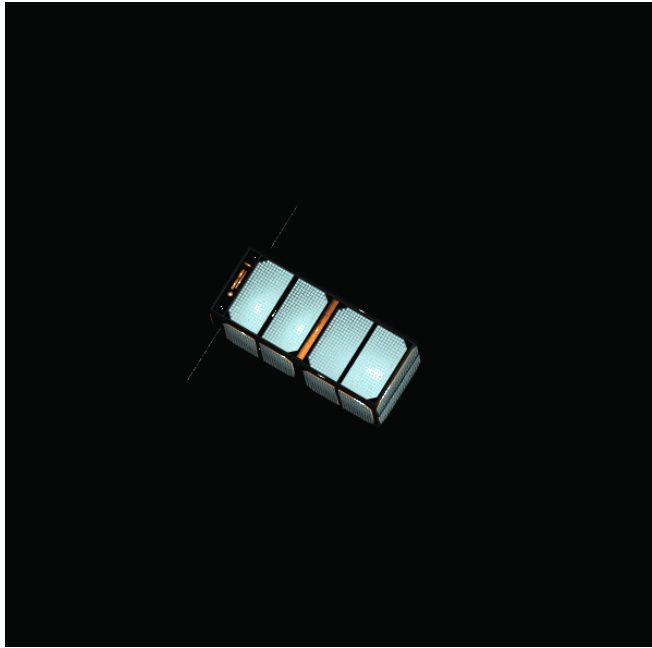


**Figure 18.** A rendered image of a 2U cubesat.

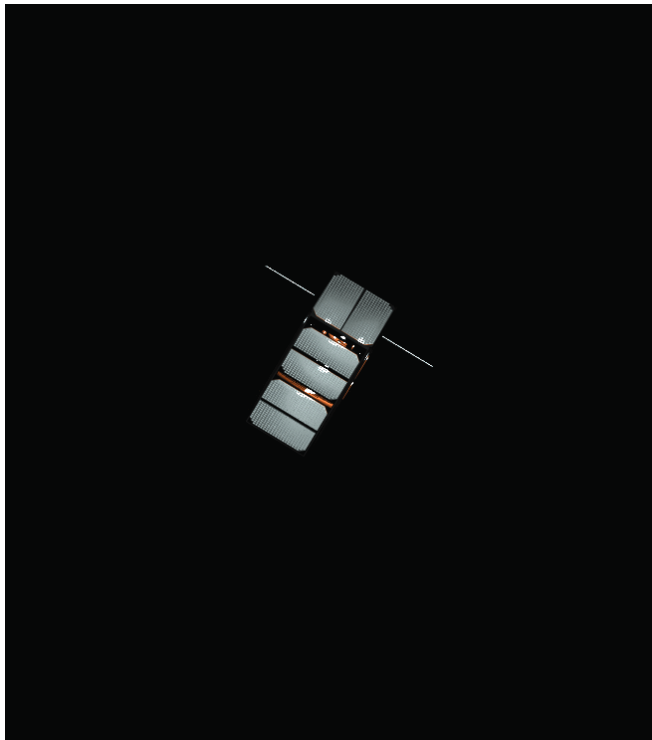


**Figure 19.** A rendered image of a 2U cubesat from a different orientation.

of the antennae towards the camera aperture, making them much more apparent. Interestingly, the digital camera model now shows the cubesat solar panels taking on a grayish tint as opposed to the blueish tint in Figure 18.

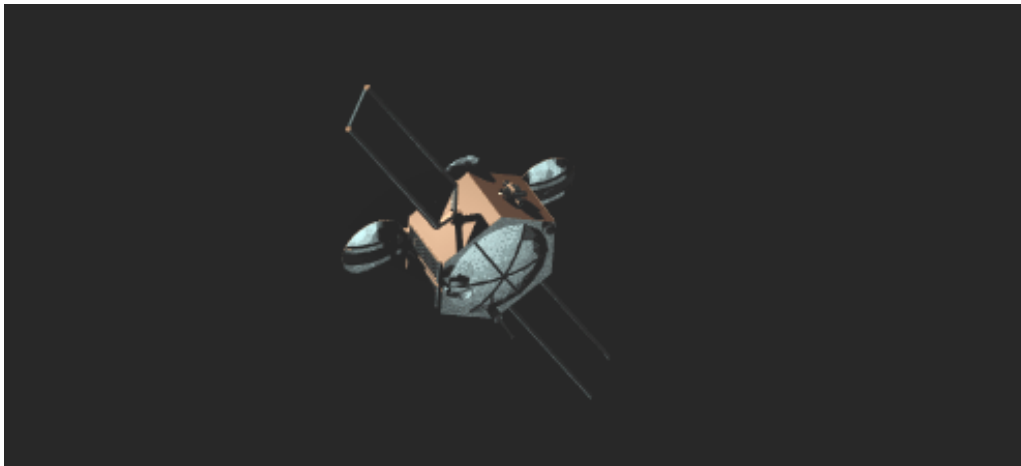


**Figure 20.** A rendered image of a generic satellite as it tumbles.

To illustrate an more complex object, a generic satellite model was textured with BRDF textures such as MLI, Aluminized Kapton, WS Gloss, and Thermbright. Imagery of this satellite rendered using DIRSIG 4 and our digital camera model can be seen in Figure 20. The object was simulated as it spun about its center about a randomized axis. A single pose can be seen in the figure in which there is almost no glint off of the solar panel wings and several facets of the object are self-shadowed. Some basic algorithms were written to track features of this spacecraft as it spun and the camera remained at a fixed orientation relative to the satellite's center. It was found that the combination of self-shadowing, and glints off of materials made this a difficult task. The use of datasets generated using DIRSIG can potentially be valuable for efforts in using computer vision and machine learning techniques for assessing the tumbling rates of non-cooperative satellites for purposes of satellite cleanup efforts (Dor & Tsiotras 2018; Oumer & Panin 2012).

## 6. CONCLUSIONS

This paper demonstrated an approach for utilizing empirical measurements of material BRDF properties for studying signatures of resolved and non-resolved RSOs. Using commercial-off-the-shelf components, we designed a goniometer system capable of characterizing the directional reflectance characteristics of spacecraft materials in the principal plane of scattering. We then utilized this goniometer system to measure the spectral BCRF of a subset of 20 different material samples that are frequently used in spacecraft design, including several different flavors of Kapton and glass reinforced polymers. The empirical BCRF measurements of these materials were then spectrally weighted using standard photometric filters to generate the photometric BCRF of the material. The empirical measurements were then fit to a Ward BRDF model using a two-step evolutionary algorithm to determine the optimal fitting parameters for describing the material's BRDF at an infinite number of viewer/illuminator geometries. Finally, we demonstrated initial results at simulating radiometrically accurate imagery of resolved and unresolved RSOs. These efforts can ultimately be extended to tasks including (1) generating large scale machine learning datasets for tasks such as pose estimate, or (2) generating more accurate BRDF models of materials that better incorporate macro-facet self-shadowing and multiple scattering.

This study will be built upon and elaborated on in future works. We ultimately plan to upgrade the goniometer system to measure non-principal-plane scattering and to better collimate the incident light

onto the target material. We also plan on doing a study on the optimal BRDF models for materials such as Kevlar that have a forward scattering lobe that does not peak in the specular direction or materials such as GFRP that exhibit a back-scattering lobe. Finally, we will age the samples using laboratory measurements and re-measure the BCRF of the samples in order to determine the changes in (1) the directional scattering of the materials and (2) their spectral characteristics.

## 7. ACKNOWLEDGMENTS

This work has been funded by Georgia Tech Research Institute Internal Research and Development (IRAD) funding. We would like to thank the thank Mr. Timothy R. Scott from DuPont de Nemours, Inc., for providing materials of the Kapton® family for this research.

## APPENDIX

### A. CHARACTERIZATION OF LIGHT SOURCE SOLID ANGLE

Our light source system that was introduced in Section 2.1 is meant to minimize the angular spread of the light source. Measuring the solid angle is an important metric to characterize the optical assembly's ability to achieve this.

The solid angle is measured in units of steradians. The solid angle subtended by an object is equal to the area of the segment of a unit sphere that the object covers (Nicodemus & FE 1977). The solid angle for a sphere of any radius can be described by the following equation:

$$\Omega = A/d^2, \tag{A1}$$

where the  $A$  is the surface area of the object projected onto the sphere and  $d$  is the radius of the considered sphere.

In order to determine the solid angle of our optical assembly with imprecise knowledge of origin of the beam, we can employ a simple derivation by measuring the light source projected area at two different locations along the optical axis (denoted by the dashed line in Figure 2). The solid angle of the light source at the closer location to the camera lens can be computed in units of steradians according to:

$$\Omega_1 = A_1/d_1^2 = \pi r_1^2/d_1^2, \tag{A2}$$

where  $r_1$  is the radius of the approximately circular beam projected onto the target plane, and  $d_1$  is the distance along the optical axis from the target plane to the effective beam origin of our optical assembly.

Using the same idea, the solid angle of the light source at a second *farther* location along the optical axis is given by  $\Omega_2 = \pi r_2^2/d_2^2$ . A diagram of this concept can be seen in Figure 21. We note that the solid angle at the two locations are equal measures of the beam expansion such that  $\Omega_1 = \Omega_2 = \Omega_b$ , where  $\Omega_b$  is the solid angle subtended by the beam.

The distances from the point source of our system to the projected beams ( $d_1$  and  $d_2$ ) are not directly known because we do not directly know the beam origin location. We therefore define two different equations to substitute in for these variables:

$$d_2 = d_1 + \Delta d \tag{A3}$$

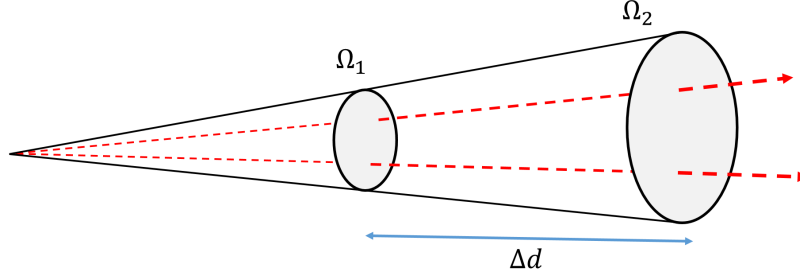


**Figure 21.** The solid angle characterization scheme. The area of the subtended beam is measured at two locations along the optical axis, giving two equivalent solid angle measurements of  $\Omega_1$  for the nearer location to the beam origin and  $\Omega_2$  for the farther location from the beam origin.

$$d_1 = \sqrt{A_1/\Omega_b} \quad (\text{A4})$$

Where  $\Delta d$  is the distance between the measured beam radii at the two points along the optical axis.

Substituting these equations into Equation A2 yields:

$$\Omega_b = \frac{A_2}{\left(\sqrt{A_1/\Omega_b} + \Delta d\right)^2} \quad (\text{A5})$$

Simplifying this equation yields:

$$\Omega_b \Delta d^2 + 2\sqrt{\Omega_b A_1} \Delta d + (A_1 - A_2) = 0 \quad (\text{A6})$$

We define the term  $\Delta A = A_2 - A_1$  to be the difference between the larger beam projection and the smaller beam projection. Substituting this term into Equation A6 and simplifying, we obtain:

$$\Omega_b^2 \Delta d^4 + \Omega_b [-2\Delta d^2(\Delta A + 2A_1)] + \Delta A^2 = 0 \quad (\text{A7})$$

$$\Omega_b^2 \Delta d^4 + \Omega_b [-2\Delta d^2(A_2 + A_1)] + \Delta A^2 = 0 \quad (\text{A8})$$

The above term can be solved using the quadratic equation for the beam solid angle,  $\Omega_b$ :

$$\Omega_b = \frac{\Delta d^2 (\Delta A + 2A_1) \pm \sqrt{\Delta d^4 (\Delta A + 2A_1)^2 - 4\Delta d^4 \Delta A^2}}{2\Delta A^2} \quad (\text{A9})$$

In summary, this method allows us to determine the beam solid angle of our light source even with an undefined beam origin using only two measurements:

1. The subtended areas of the beam at two different locations along the optical axis of the system, with  $A_1$  being the projected area of the beam at a closer location to the camera lens in Figure 2 and  $A_2$  being the projected area at a farther location.
2. The distance between the two measured areas along the optical axis,  $\Delta d$ .

## REFERENCES

- |   |   |
|---|---|
| <p>Badura, G., Valenta, C. R., &amp; Gunter, B. 2020, Advanced Maui Optical and Space Surveillance Technologies Conference (AMOS)</p> | <p>Bedard, D., Lévesque, M., &amp; Wallace, B. 2011, in Proc. of the Advanced Maui Optical and Space Surveillance Technologies Conf, 1–10</p> |
|---|---|

- Bédard, D., Wade, G. A., & Abercromby, K. 2015, *Journal of Spacecraft and Rockets*, 52, 1038
- Bennett, D. A., Dank, J. A., Tyler, D. W., Gartley, M., & Allen, D. 2014, in *Advanced Maui Optical and Space Surveillance Technologies Conference*. URL: <http://www.amostech.com/TechnicalPapers/2014/Poster/BENNETT>
- Beveridge, A., Fung, T., & MacDougall, D. 2001, *Forensic examination of glass and paint: Analysis and interpretation*, 220
- Budding, E., & Demircan, O. 2007, *Introduction to astronomical photometry*, Vol. 6 (Cambridge University Press)
- Clark, R. N., Swayze, G. A., Livo, K. E., et al. 2003, *Journal of Geophysical Research: Planets*, 108
- Clark, R. N., Swayze, G. A., Leifer, I., et al. 2010, *US Geological Survey open-file report*, 1167, 1
- Clegg, R., Jolliff, B., Robinson, M., Hapke, B., & Plescia, J. 2013, in *Lunar and Planetary Science Conference No. 1719*, 2171
- Cowardin, H. M., Hostetler, J. M., Murray, J. I., Reyes, J. A., & Cruz, C. L. 2020, in *Advanced Maui Optical and Space Surveillance Technologies Conference (AMOS)*, Maui, HI
- Denevi, B. W. 2011, in *EPSC-DPS Joint Meeting 2011*, Vol. 2011, 1238
- Dianetti, A. D., & Crassidis, J. L. 2018, in *2018 AIAA Guidance, Navigation, and Control Conference*, 1605
- Dor, M., & Tsiotras, P. 2018, in *2018 Space Flight Mechanics Meeting*, 1963
- Farrell, J. E., Catrysse, P. B., & Wandell, B. A. 2012, *Applied optics*, 51, A80
- Furfaro, R., Linares, R., & Reddy, V. 2018, in *AMOS Technologies Conference*, Maui Economic Development Board
- Gaffey, M. J., Burbine, T. H., & Binzel, R. P. 1993, *Meteoritics*, 28, 161
- Gazak, J. Z., Fletcher, J., Swindle, R., & McQuaid, I. 2020
- Goodenough, A. A., & Brown, S. D. 2012, in *Algorithms and Technologies for Multispectral, Hyperspectral, and Ultraspectral Imagery XVIII*, Vol. 8390, International Society for Optics and Photonics, 83900H
- Harms, J. D., Bachmann, C. M., Ambeau, B. L., et al. 2017, *Journal of Applied Remote Sensing*, 11, 046014
- Ientilucci, E. J., & Brown, S. D. 2003, in *Targets and Backgrounds IX: Characterization and Representation*, Vol. 5075, International Society for Optics and Photonics, 110–121
- Kokaly, R. F., Asner, G. P., Ollinger, S. V., Martin, M. E., & Wessman, C. A. 2009, *Remote Sensing of Environment*, 113, S78
- Li, H., Foo, S.-C., Torrance, K. E., & Westin, S. H. 2006, *Optical Engineering*, 45, 043605
- Li, X., & Strahler, A. H. 1992, *IEEE transactions on Geoscience and Remote Sensing*, 30, 276
- Miranda, L. J. V., et al. 2018, *J. Open Source Software*, 3, 433
- Moré, J. J. 1978, in *Numerical analysis* (Springer), 105–116
- Ngan, A., Durand, F., & Matusik, W. 2005, *Rendering Techniques*, 2005, 2
- Nicodemus, F. E., & FE, N. 1977
- Oumer, N. W., & Panin, G. 2012, in *Proceedings of the 21st International Conference on Pattern Recognition (ICPR2012)*, IEEE, 796–800
- Schaepman-Strub, G., Schaepman, M. E., Painter, T. H., Dangel, S., & Martonchik, J. V. 2006, *Remote sensing of environment*, 103, 27
- Schott, J. R., Brown, S. D., Raqueno, R. V., Gross, H. N., & Robinson, G. 1999, *Canadian Journal of Remote Sensing*, 25, 99
- Shi, Y., & Eberhart, R. 1998, in *1998 IEEE international conference on evolutionary computation proceedings. IEEE world congress on computational intelligence* (Cat. No. 98TH8360), IEEE, 69–73
- Sparks, W. B., & Ford, H. C. 2002, *The Astrophysical Journal*, 578, 543
- Walter, B. 2005, *Program of Computer Graphics*, Cornell University, Technical report PCG-05, 6
- Ward, G. J. 1992, in *Proceedings of the 19th annual conference on Computer graphics and interactive techniques*, 265–272